

Journal Pre-proofs

Reconfigurable Surfaces Employing Linear-Rotational and Bistable-Translational (LRBT) Joints

Yang Li, Anjini Chandra, Charles J. Dorn, Robert J. Lang

PII: S0020-7683(20)30379-6
DOI: <https://doi.org/10.1016/j.ijsolstr.2020.09.029>
Reference: SAS 10861

To appear in: *International Journal of Solids and Structures*

Received Date: 19 June 2020
Revised Date: 15 September 2020
Accepted Date: 22 September 2020

Please cite this article as: Y. Li, A. Chandra, C.J. Dorn, R.J. Lang, Reconfigurable Surfaces Employing Linear-Rotational and Bistable-Translational (LRBT) Joints, *International Journal of Solids and Structures* (2020), doi: <https://doi.org/10.1016/j.ijsolstr.2020.09.029>

This is a PDF file of an article that has undergone enhancements after acceptance, such as the addition of a cover page and metadata, and formatting for readability, but it is not yet the definitive version of record. This version will undergo additional copyediting, typesetting and review before it is published in its final form, but we are providing this version to give early visibility of the article. Please note that, during the production process, errors may be discovered which could affect the content, and all legal disclaimers that apply to the journal pertain.

© 2020 Elsevier Ltd. All rights reserved.



Reconfigurable Surfaces Employing Linear-Rotational and Bistable-Translational (LRBT) Joints

Yang Li^{a, b, *}, Anjini Chandra^c, Charles J. Dorn^b, Robert J. Lang^d

^a *The Institute of Technological Sciences, Wuhan University, Wuhan 430072, PR China*

^b *Graduate Aerospace Laboratories, California Institute of Technology
1200 E. California Blvd, Pasadena, CA 91125, United States*

^c *California Institute of Technology*

1200 E. California Blvd, Pasadena, CA 91125, United States

^d *Lang Origami, Altadena, CA 91001, United States*

Abstract

Reconfigurable surfaces are useful in many applications. This paper proposes a type of reconfigurable surfaces that consist of rigid elements (tiles) connected by novel compliant joints. Depending on the actuation, these novel connecting joints can either operate as torsional hinges, which create isometric transformation (like origami folding) between connected tiles, or bistable translational springs, which accommodate metric-changing transformation between connected tiles. A specific example of a reconfigurable surface with square tile shape that can morph into flat, cylindrical (in two different directions), and spherical configurations with simple actuation is given.

Keywords: reconfigurable structures, isometric transformation, origami, torsional hinges, metric-changing transformation, bistability, compliant mechanisms

*Corresponding author. Email: yang.li@whu.edu.cn

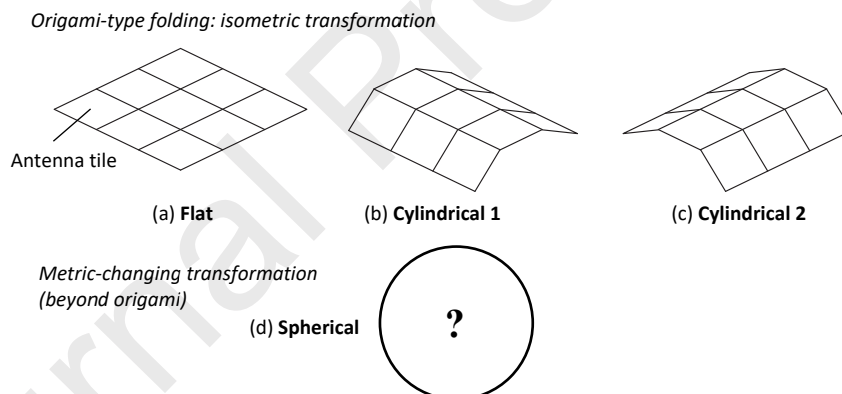
1. Introduction

Reconfigurable surfaces are useful for applications that require several service configurations, which can lead to more powerful and compound devices. The application that this paper corresponds to is for an antenna that has a mechanically reconfigurable platform. Such platforms can help the antennas to adjust polarization [1], frequency of active antennas [2-5] and of passive ones [6-8], and their radiation pattern [9-13] through active mechanical reconfiguration. A mechanically reconfigurable platform can also make the antenna deployable so that it is easier to be transported [14-18].

This paper aims at providing a mechanically reconfigurable platform for a novel antenna array concept introduced in [19], in which it breaks the trade-off between steering range, i.e., field of view, and directivity, i.e., fidelity in a specified direction. Traditionally, a phased array antenna with a flat configuration has high fidelity in the normal direction but a rather narrow field of view, and a conformal antenna on a curved surface can have a large field of view but relatively low fidelity [20]. This is due to the well-known property that directivity is proportional to cross-sectional areas for large arrays [21, 22]. A novel concept to combine the merits of the two through mounting antenna tiles on a mechanically reconfigurable platform was proposed in [19].

Specifically, the platform needs to morph in between flat (the highest fidelity in the normal direction while the narrowest field of view), cylindrical 1 and 2 (a wider field of view in two different directions while correspondingly lower fidelity), and spherical (the widest field of view in all directions and the lowest fidelity) configurations, as shown in

Figure 1 where the spherical configuration is unknown and is proposed in this paper. As a result, the field of view and the directional fidelity of the antenna can be tuned during service through mechanical reconfiguration. Figure 1(a)-(c) involve isometric transformation, i.e., the distances (following the surface) between nodes are not changing, and Figure 1(d) involves metric-changing transformation, i.e., extensions of distances (following the surface) between nodes are needed. This paper proposes the design method for the reconfigurable surface that satisfies the requirement shown in Figure 1 while achieving easy manufacturability, simple actuation, and high stiffness. The detailed antenna concept and properties will be reported separately in [19].



65 Figure 1. Four target morphing configurations to be achieved by the mechanically reconfigurable surface.

Active origami can be used to generate reconfigurable surfaces. Most existing work is limited to isometric morphing [23-25], where only folding deformation is involved. Furthermore, these patterns are typically one degree-of-freedom (DOF) origami patterns, such as Miura-

ori [26], which are most popular due to their simplicity to control. More sophisticated origami patterns like the waterbomb base [27] and Resch's pattern [28] can provide metric-changing morphing if only tracking the overall shape (only considering certain tiles). For instance, these origami patterns can morph from flat to spherical configurations. However, complex fold patterns introduce prohibitive manufacturing challenges and lead to high DOF structures requiring complex actuation [29, 30]. Another similar technique is to use kirigami and extensible elements to achieve metric-changing transformation and reconfigure a flat plane to a 3D surface [31-33], but the tile or nodal arrangement cannot be aligned as shown in Figure 1 and provide the required isometric deformation.

Alternatively, active elastomers can produce both isometric and metric-changing deformation. Through manipulation of the magnetic [34], electrical [35], heat [36, 37], or humidity [38] field, active elastomers can produce differential swelling in different directions and correspondingly generate designed overall deformation. However, compared to active origami, active elastomers generate relatively small curvature change with slow actuation response, and their low stiffness is problematic for maintaining shape in operation as a morphing platform.

Another method is to discretize the surface and control each part individually [39, 40], which can provide the most flexible reconfiguration comparing to active origami and active elastomers. However, this method is heavy, expensive, and unnecessary for applications that require only certain specified reconfigurations (such as those described in Figure 1).

The solution proposed in this paper is to design the connection between square tiles that can work as (1) a torsional hinge to provide isometric transformation (origami-like folding) and (2) a bistable translational spring to accommodate metric-changing transformation that can only be initiated when the energy barrier (due to the bistability) is overcome. Global bi/multistability can simplify the actuation [41] during metric-changing transformation. From the literature, lamina emergent torsional (LET) joints [42, 43] can produce integrated torsional hinges, and snap-through slender beams [32, 44, 45] can provide bistable translational springs. This paper proposes the integration of the two, which will be referred to as linear-rotational and bistable-translational (LRBT) joints. In consequence, it is possible to build an isometric and metric-changing reconfigurable surface that has easy manufacturability (by simply cutting a plate), is easy to actuate (due to the bistability), and is sufficiently stiff (due to the bistability) to maintain shape.

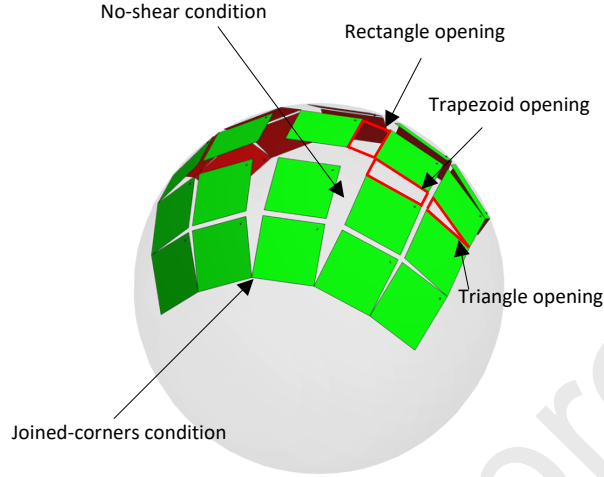
This method can be generalized for other tile shapes and target morphing configurations, which leads to wider applications. Multiple cameras can be mounted on different tiles of a reconfigurable platform to change the overall field of view and resolution. Manufacturing 3D structures from 2D material is useful for optical sensors [46, 47], electronics [48], and so on [49], to which the LRBT joints might be applicable. Besides morphing surfaces/platforms, LRBT joints might be used for multifunctional origami robots [50, 51] where smooth motion is provided by isometric transformation while bistable metric-changing transformation can be used to provide the reconfigurable for different functions or directional propulsion [52].

This paper is laid out as follows. Section 2 presents a deterministic procedure for arranging square tiles on a sphere to form the spherical configuration. Section 3 introduces the design of linear-rotational and 125 bistable-translational (LRBT) joints. As an example, Section 4 provides the design, manufacturing, and actuation of reconfigurable surfaces employing the square tessellation on a sphere and LRBT joints. Section 5 concludes the paper.

130

2. Arrangement of Squares on a Sphere

Since a plane, cylinder 1, and cylinder 2 (Figure 1(a)-(c)) are all developable surfaces, they can all be realized by simple folding (or not folding) of an initially planar shape. Achieving a spherical configuration 135 from an initially planar arrangement of square tiles is more challenging, though. Because a sphere has nonzero Gaussian curvature, the deformation from the plane to the sphere must be non-isometric, or, in simpler terms, the spacing between adjacent tile pairs must vary from tile to tile, as illustrated in Figure 2.



140

Figure 2. Arrangement of square tiles on a sphere to achieve the fourth target configuration (spherical).

145 We assume a sphere of radius R and use unit square tiles. Define

$$x_0 = \frac{1}{2}, \quad z_0 = \sqrt{R^2 - \left(\frac{1}{2}\right)^2}. \quad (1)$$

Since the tiles form a square grid, we index the tiles on two indices (i, j) , with the $(0, 0)$ th tile located at the “North Pole” of the sphere. For each tile, we define the four corner coordinates in clockwise order, and distinguish them by adding a third index $k \in [1, \dots, 4]$, as illustrated in

150 Figure 3(a). For the $(0, 0)$ th tile, the four vertices are

$$\mathbf{P}_{0,0,1} = (x_0, x_0, z_0), \quad (2)$$

$$\mathbf{P}_{0,0,2} = (-x_0, x_0, z_0), \quad (3)$$

$$\mathbf{P}_{0,0,3} = (-x_0, -x_0, z_0), \quad (4)$$

$$\mathbf{P}_{0,0,4} = (x_0, -x_0, z_0). \quad (5)$$

We can construct a local frame of unit vector $(\mathbf{x}_{i,j}, \mathbf{y}_{i,j}, \mathbf{z}_{i,j})$ for each tile, where $\mathbf{x}_{i,j}$ points from the center of the tile to the first edge and is perpendicular to it; $\mathbf{y}_{i,j}$ points from the center of the tile to the second edge and is perpendicular to it; and $\mathbf{z}_{i,j}$ is normal to the tile. For the (0, 0)th tile, the local frame is

$$\mathbf{x} = (1, 0, 0), \quad \mathbf{y} = (0, 1, 0), \quad \mathbf{z} = (0, 0, 1). \quad (6)$$

A tile anywhere on the sphere can be parameterized on three angles that describe a transformation of the tile from the position of the (0, 0)th tile:

- $\psi_{i,j}$, an initial rotation of the tile about the z -axis;
- $\theta_{i,j}$, an azimuthal rotation of the tile from the North Pole down to a lower latitude;
- $\phi_{i,j}$, an axial rotation of the tile about the z -axis to a different longitude.

We define the transformation of a vector $\mathbf{q}_{i,j}$ in terms of arbitrary $(\theta_{i,j}, \phi_{i,j}, \psi_{i,j})$ by

$$\mathbf{a}_{i,j} = \left(\cos\left(\phi + \frac{\pi}{2}\right), \sin\left(\phi + \frac{\pi}{2}\right), 0 \right), \quad (7)$$

$$\mathbf{n}_{i,j} = (\sin \theta \cos \phi, \sin \theta \sin \phi, \cos \theta), \quad (8)$$

$$\mathbf{q}_{i,j} = \mathbf{R}(\phi, \mathbf{n}) \cdot \mathbf{R}(\theta, \mathbf{a}) \cdot \mathbf{q}_{0,0}, \quad (9)$$

165 where $\mathbf{R}(\alpha, \mathbf{u})$ is the 3D rotation through angle α about axis \mathbf{u} . $\mathbf{q}_{i,j}$ can represent either a vertex corner vector $\mathbf{P}_{i,j,k}$ or a local frame vector $\mathbf{x}_{i,j}$, $\mathbf{y}_{i,j}$, or $\mathbf{z}_{i,j}$.

We can simplify the problem by assuming mirror symmetry along the reflection axes of a square, in which case we only need to solve for a subset of the tiles. If we specify a $(2n + 1) \times (2n + 1)$ array, we need
170 to solve only for the tiles within indices $i = 0, \dots, n$, $j = 0, \dots, i$, as illustrated in Figure 3.

We set up the problem of finding tiles positions as a constrained optimization, where the variables being constrained are the three angles
175 for each tile (via the tile corners parameterized on them), and the constraints are of several types:

- **Joined corners.** Because we want the largest possible fill factor, we want no excess gaps between tiles. We achieve this by choosing that the corners of adjacent tiles along the outside ring
180 are joined.
- **No shear.** In order to reduce the number of design variables, we adopt the *no-shear* condition on adjacent tiles.

For the joined-corners constraint, a simple constraint that specifies joining would be to require that the distance between the pair of corners
185 to be joined be set equal to zero. However, this is numerically fragile; it is equivalent to finding the zero of a function by minimizing its absolute value. Instead, we should like to find a multidimensional function whose value goes through zero smoothly.

We achieve this by expressing the coordinates of one of the corners to
190 be joined in the local frame of the tile of the other coordinate, and then

requiring that the local x and y coordinates match. (There is no need to match the z coordinates because the vertices are already on the surface of the sphere.) Thus, if we denote the two corners to be forced to join by \mathbf{P}_{i_1,j_1,k_1} and \mathbf{P}_{i_2,j_2,k_2} , we have two equality constraints to enforce point
 195 coincidence:

$$(\mathbf{P}_{i_1,j_1,k_1} - \mathbf{P}_{i_2,j_2,k_2}) \cdot \mathbf{x}_{i_1,j_1} = \mathbf{0}, \quad (10)$$

$$(\mathbf{P}_{i_1,j_1,k_1} - \mathbf{P}_{i_2,j_2,k_2}) \cdot \mathbf{y}_{i_1,j_1} = \mathbf{0}. \quad (11)$$

The no-shear condition arises from the preference to reduce the number of design variables (for arranging squares on a sphere) and regulate the relative motion between square tiles (so that shapes of opening are easier to categorize). If we denote the vertices of the two
 200 tiles as \mathbf{P}_A , \mathbf{P}_B , \mathbf{P}_C , and \mathbf{P}_D , then the no-shear condition for that particular pair is simply

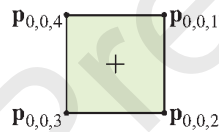
$$\|\mathbf{P}_A - \mathbf{P}_C\| - \|\mathbf{P}_B - \mathbf{P}_D\| = 0. \quad (12)$$

The joined-corners and no-shear conditions form the constraints of the optimization.

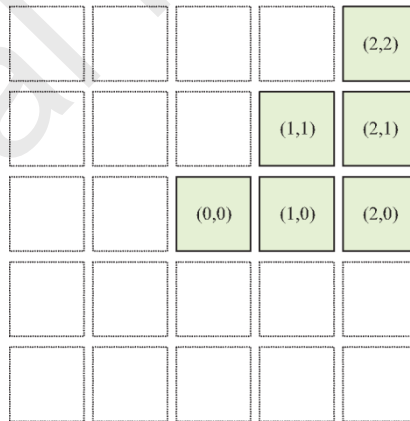
For the figure of merit, we use the goal that we would like the tiles to
 205 be as evenly spaced as possible; a way of achieving this is to choose the root mean square (RMS) sum of the distances between adjacent pairs of vertices to be zero (since using RMS sum of spacing of elements confined to a finite region will, all else being equal, drive the spacing to be roughly equivalent). In fact, as it turns out, other constraints of the
 210 spherical geometry force distinctly unequal spacing, but choosing the

RMS goal has the effect of “soaking up” any excess degrees of freedom in the system, leading to a definite (numerical) solution for the positions.

We optimize over the angle variables $(\theta_{i,j}, \phi_{i,j}, \psi_{i,j})$ for the (i, j) values of the tiles in the minimal set, using symmetry to find the coordinates for any other tile vertices involved in the constraints or figure of merit. Note that the positions of the joined corners are not placed: they are determined from the solution of the system of equations. There is no guarantee of a solution; for any given number of tiles, there is a minimum sphere size for which a solution can be found. (This is obvious from the fact that at some point, the area of the sphere is going to be less than the area of the set of tiles.)



(a) Labeling of the four vertices of a tile



(b) Schematic of a $(2n + 1) \times (2n + 1)$ array of tiles with indices (i, j) ; only the shaded tiles have independent variables to be solved for

Figure 3. Labeling of vertices and tiles.

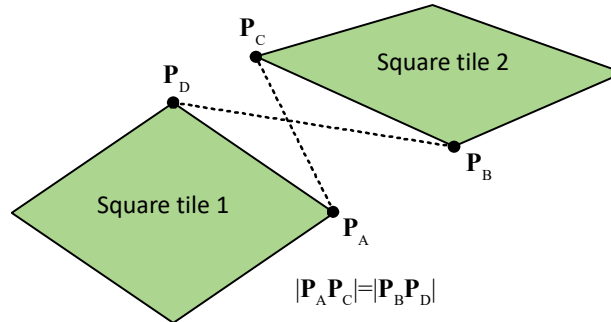


Figure 4. No-shear condition between adjacent square tiles to reduce design parameters.

235 We parameterize each tile in terms of three variables: the altitude and azimuth of the centroid of the tile and the relative rotation of the tile about its centroid. An overall design parameter is the sphere radius (we assume unit square tiles). From those parameters, we can compute the four vertices of each tile; from the vertices, we can construct our FOM and
 240 the no-shear and joined-corner condition constraint equations. We then solve this system of equations (using *Mathematica*) to find the tile arrangement shown in Figure 2, and this method is used in the rest of this paper.

245 The resultant openings between square tiles can be categorized as rectangle, triangle, and trapezoid shapes as shown in Figure 2. Bistable-translational elements were then designed accordingly, as described in the next section.

3. Introduction of Linear-Rotational and Bistable-Translational (LRBT) Joints

250

In this section, joints that connect square tiles that can in one hand provide rotation along the edge of squares for isometric transformation, as shown in Figure 1(a)-(c), and in the other hand can provide translation between squares for metric-changing transformation, as shown in Figure 2, are introduced. They are categorized into rectangle, triangle, and trapezoid openings based on their target open shapes.

255

3.1 The Rectangle Opening LRBT Joints

3.1.1 Geometry and Deformation

Consider two plates that are connected by four slightly curved elastic beams in 2D, as shown in Figure 5(a), where end connections of those beams have thinner profiles so that rotation can occur easily. The out of plane thickness of the material $t = 3.175$ mm. The material used is polypropylene copolymer. Tensile tests were performed, and the material stress-strain curve is given in Figure 6. The properties of the polypropylene copolymer are as follows: density = 10^{-3} g/mm³, Young's modulus = 322 MPa, Poisson's ratio = 0.3, yield stress = 24 MPa, yield strain $\epsilon_y = 7.5\%$, and the elongation before break is 650%.

260

265

3.1.1.1 Bistability in Translation

The in-plane translational (extensional and compressional) behavior of LRBT hinges was modeled in Abaqus/Explicit [53] using 85736 C3D8R elements. A convergence test of mesh density was conducted, and the

270

kinetic energy and artificial energy of all simulations were well below 5% of the total energy. Linear elasticity and plasticity (input the curve in Figure 6 into Abaqus) were considered in the material model. Viscosity of the material was not included because simple material tests (without varying and recording strain rates) were employed as the numerical model is to only capture the main feature (the LRBT effect) of the joint. In the simulation, the left side of the structure was clamped, and a horizontal displacement was imposed to the right side of the structure. The prescribed displacement was 11 mm applied over a 0.5 s interval. This is noted as *stage 1*, in which the structure was pulled open as shown in Figure 5(b). The displacement was then reversed back to 0 mm over 0.5 s; this is noted as *stage 2*. In these two stages, plastic deformation only occurred in the joining area to form living hinges while the rest of the beams remained elastic, as shown in Figure 5(c).

The same displacement was imposed experimentally by an Instron machine with a speed of 5.5 mm/min. The experimental deformation is shown in Figure 5(b). Three test samples were manufactured by laser cutting a 3.175 mm thick polypropylene sheet.

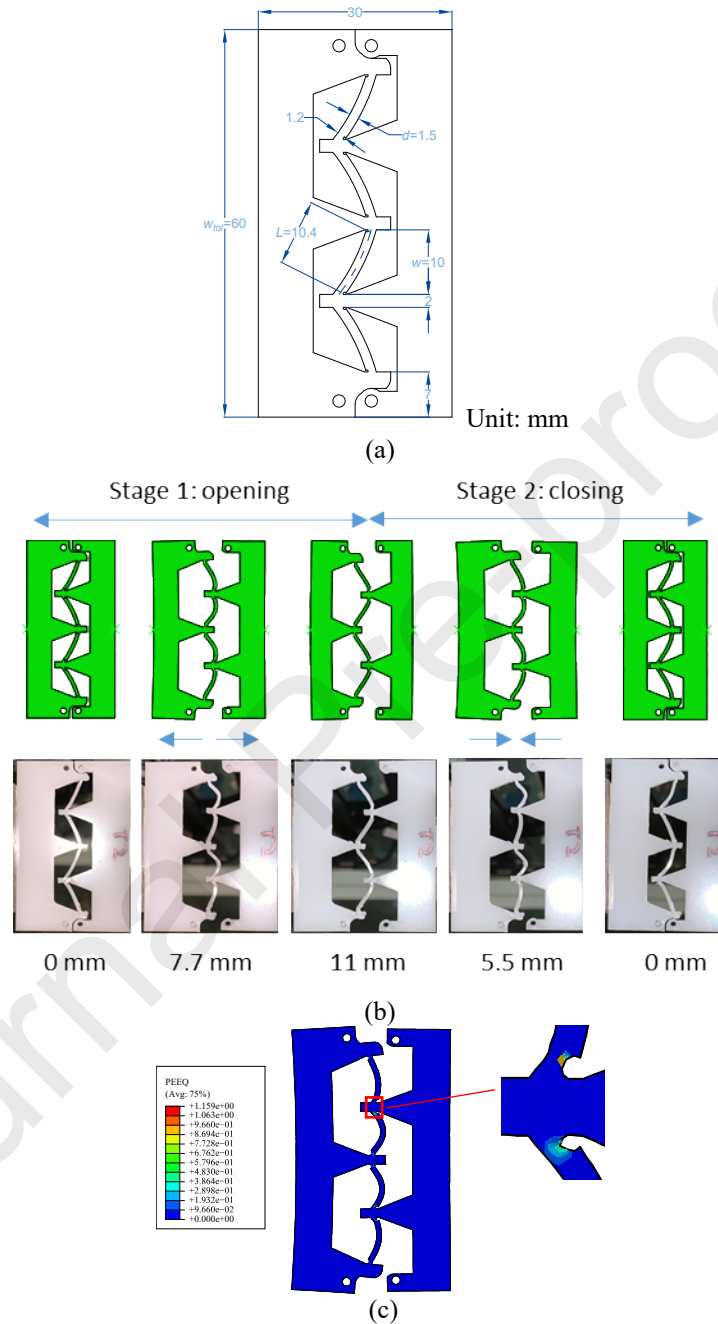


Figure 5. A rectangle LRBT element: (a) schematic drawing with dimensions, (b) deformation given in numerical simulation and experiment with respective displacements of 0 mm, 6.5 mm, 11 mm, 6.5 mm, and 0 mm, and (c) plastic deformation in the connection hinges that forms living hinges.

295

300

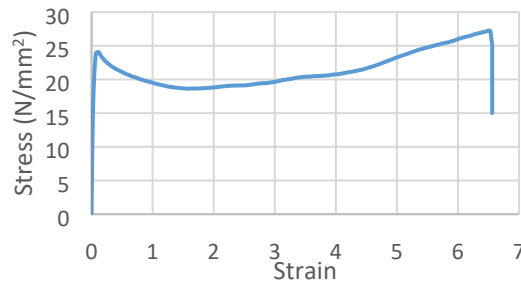


Figure 6. The uniaxial stress-strain curve of polypropylene copolymer.

305 Energy and reaction force plots of this process are given in Figure 7. As shown in Figure 6, the material is softened in the plastic region. This is reflected in Figure 7, where the plastic energy is flatter in stage 2 when the displacement is decreasing. This indicates that localized and soft plastic living hinges are formed in the end connections of those beams
 310 (noted in Figure 5(c)). In consequence, two stable states can be observed in stage 2 according to internal energy, elastic energy, and reaction force. The slight deviation of stable positions between internal energy (or reaction force) and elastic energy is due to the existence of plastic hinges (residual moments). As a result, the structure (after the formation of
 315 plastic living hinges) is bi-stable in the translational deformation. Both stable configurations occur when the elastic beams are undeformed (with slight drifting due to plastic hinges). Plots of numerical and experimental reaction forces in Figure 7 show almost identical stable positions in stage 2. Experimental reaction forces of the three samples show good
 320 consistency as noted by the error bars. However, they have overall different magnitude to the numerical reaction force in Figure 7(b). The difference is significant in stage 1 where plastic living hinges are in the

process of forming which is not well captured by the simulation, while stage 2 shows a closer match. The experimental reaction force at the displacement of 11 mm is significantly the highest, which indicates the beams are practically shorter than the design due to manufacturing inaccuracy and the effect of beam width. As a result, the beams are in tension at the displacement of 11 mm in experiments, and the plot shows a sharp increase of reaction force. Additionally, the lack of consideration of viscous effects in the numerical model can also contribute to this deviation.

Cyclic loading (with 4 cycles in total and the same speed) was tested experimentally and has shown that the sample is repeatedly bistable after the first half of the initial cycle where plastic hinges or living hinges (noted in Figure 5(c)) are formed. Differences between the reaction forces of stage 1 and 2 were mainly caused by viscoelasticity.

Elastic energy during the stage 2 in the numerical simulation captures the inherent bistability better than the internal energy which includes the plastic energy that shifts the stable positions differently depending on the loading history/direction. In consequence, elastic energy is used in later sections to characterize the translational bistability of other LRBT joints.

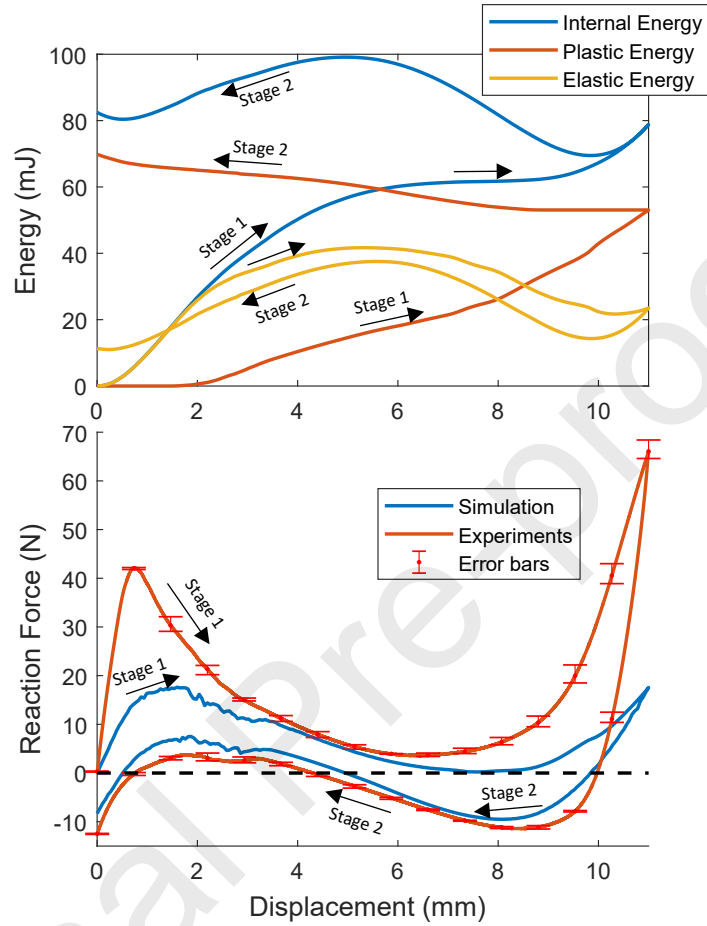


Figure 7. Plots of energy (from simulation) and reaction force (from simulation and experiments) to the displacement of stage 1 (pulling from 0 mm to 11 mm) and stage 2 (compressing from 11 mm to 0 mm) of a rectangle LRBT joint.

345

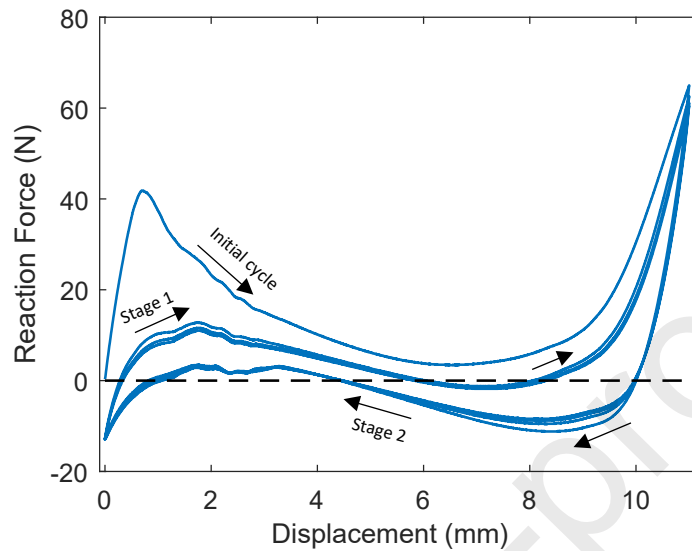


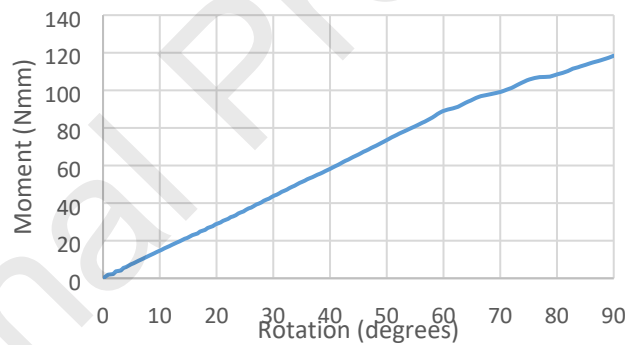
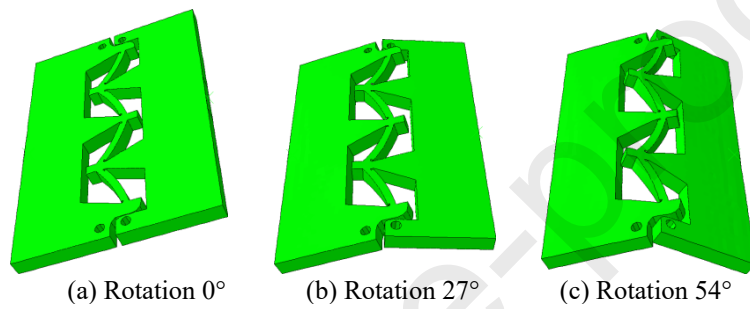
Figure 8. Plots of the experimental reaction force to the displacement in a cyclic loading (between 0 mm and 11 mm displacement) of a rectangle LRBT joint.

350 3.1.1.2 Linear Elastic in Rotation

Consider the same structure given in Figure 5(a). Now, pure bending is applied in the numerical simulation, where the plate on the left side is clamped, and the rotation is applied to the plate on the right side, as shown in Figure 9. The total step time is 0.5 s. The hinge is linear elastic
 355 until the rotation reaches 60° , where plasticity starts to occur, as shown in Figure 9(d). This result indicates that this structure (if made of linear elastic material) shall have linear elastic bending behavior.

Experiments of 3 samples were conducted using a pure bending machine (with a accuracy of 8.9 Nmm) that has been introduced and used
 360 in [54, 55]. The experimental setup is shown in Figure 10(a), experimental bending deformation with a rotation of 40° is given in

Figure 10(b), and plots of reaction moments of 3 samples are presented in Figure 10(c). After the experiment, sample 2 and 3 slowly recovered to the flat configuration while sample 1 recovered to a residual rotation of 7°. This recovery together with plots indicates that the structure is viscoelastic within a rotation of 25°.

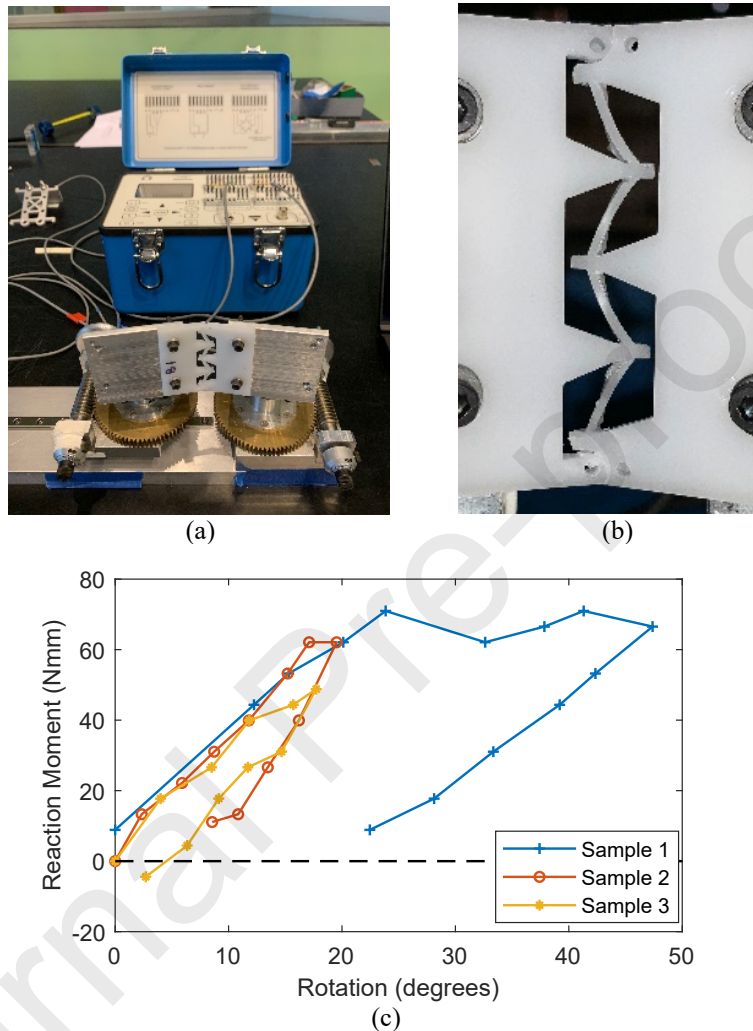


370

(d) Moment to rotation plot

Figure 9. Simulated bending deformation of a rectangle LRBT element and its moment to rotation plot.

375



380

Figure 10. Bending experiments of 3 rectangle LRBT samples: (a) the experimental setup; (b) deformation with a rotation of 40°; and (c) moment to rotation plots.

This linear elastic behavior shows that this rectangle LRBT joint works similarly to a LET joint [42]. (A LET joint is a torsional hinge with integrated beams that act as torsional springs whose stiffness is designable and governed by geometric parameters of the beams.) Numerical simulation with the same settings (mesh density, loading

385

speed, etc.) is used in Section 3.1.2, 3.2, and 3.3 and to characterize the
390 bending behavior of other LRBT joints with a linear elastic material
assignment.

The hinge-rotation does not remove the translational bistability and
does not introduce parasitic translational deformation. This is observed
in experiments and simulations, where the hinge stayed closed stably
395 during hinge-rotation. Translation of the hinge is associated with bending
deformation of beams, while rotation of the hinge is associated with
torsional deformation of beams. Intuitively, the translational bistability
is introduced by the two symmetric configurations (open and closed in
translation) where beams are almost “bending-free”. The introduction of
400 hinge-rotation does not break that symmetry so the bistability remains.
Hinge-rotation creates torsional deformation in beams, which has a
negligible translational projection. As a consequence, parasitic
translational deformation is not expected during bending.

Now we have presented a basic element that can act as a bistable
405 translational spring or a linear torsional hinge depending on the loading.
These two behaviors (translating and bending) are well separated by the
energy barrier shown in the stage 2 of Figure 7.

3.1.2 Parametric Study

To develop design guidelines for LRBT hinges, the following design
410 requirements are proposed and need to be satisfied: (a) beams are not
plastically deformed; (b) reasonable stiffness for the bistability which is
realized by introducing small initial curvature to beams; (c) the
translational deformation (snap-through of beams) remains in 2D, which

is achieved by designing beam widths significantly smaller than the
 415 material thickness. A rough analytical model is used to prevent plasticity
 in the beams during translation (except at the ends of the beams).
 Assuming the beam deforms into a circular arch, geometric parameters
 w , L (taken as the distance between end points), and d noted in Figure 5
 need to satisfy the following relationships for it to stay within the elastic
 420 region (to satisfy requirement (a)).

$$\sin\left(\frac{\theta}{2}\right) = \frac{w}{2R}, \quad (13)$$

$$L = R\theta, \quad (14)$$

$$R > \frac{d}{2\varepsilon_y}, \quad (15)$$

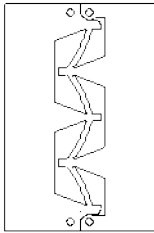
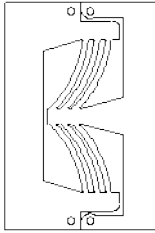
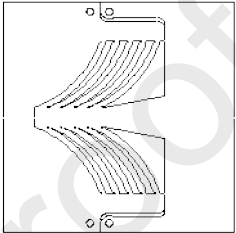
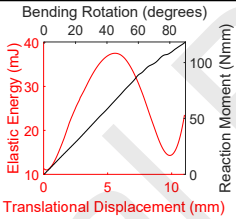
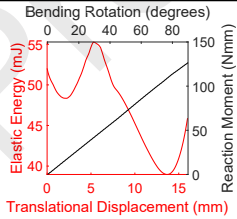
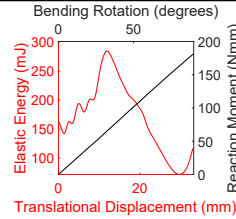
where R and θ are the radius and the central angle of the deformed beam,
 respectively. This model provides a rule of thumb for design, and has not
 considered viscosity and used simple engineering strain as the indication
 425 of yielding. For the material thickness $t = 3.175$ mm used in this study, a
 beam width $d = 1.5$ mm (to satisfy requirement (c)) and total width w_{tot}
 $= 60$ mm (to match the antenna tile size) as noted in Figure 5(a) are
 chosen for all LRBT designs in this paper.

Drawing procedures for generating rectangle LRBT joints with
 430 specified openings are given in Figure 24 in Appendix A. Designs of
 three different target rectangle openings g_r , which are 10 mm, 17 mm,
 and 32 mm are provided in Table 1 according to the principle introduced
 in Figure 24. Similar designs that are used for the 17 mm and 32 mm
 openings are previously introduced in [56], which have several pairs of

435 beams in the transverse direction of the hinge to eliminate “parasitic”
kinematics illustrated in [57]. All three design requirements are satisfied.

Two samples of each LRBT hinge design were manufactured by laser
cutter, and the averaged stable opening sizes are given in Table 1.
Manufactured samples are presented in Figure 11, which shows the
440 translational deformation (stable by elastic strain energy) and rotational
deformation (held at a fixed rotation angle by tape). They open to
approximately the designed size and rotate along the edge of two plates.
Slight deviations from the target openings are mainly caused by (1) the
occurrence of the plastic hinges is not at ends of beams so that effective
445 beam lengths are smaller and (2) deformation of elastic beams due to
residual moment at the plastic connection hinges at ends of beams.
Drawings with detailed dimensions are given in the supplementary
material. The “kerf” of the laser cutting is 0.2 mm and has been taken
into account. Translational (stage 2) and bending plots from numerical
450 simulations are given in Table 1, which shows the linear-rotational and
bistable-translational behavior for all three designs. Local fluctuations in
curves are due to contact between boundaries during gap closing. Stage
2 (in Figure 7) of their translational behavior (compression) is plotted, so
the elastic energy is not zero when the translational displacement is zero
455 due to the residual moment in the plastic living hinges.

Table 1 Three rectangle LRBT joints.

Target Opening g_r	10 mm	17 mm	32 mm
Design			
Opening size exp. (mm)	10.10	16.31	30.31
Avg. exp. error	1.02%	-4.07%	-5.30%
Num. translation (stage 2) and bending plots			

460

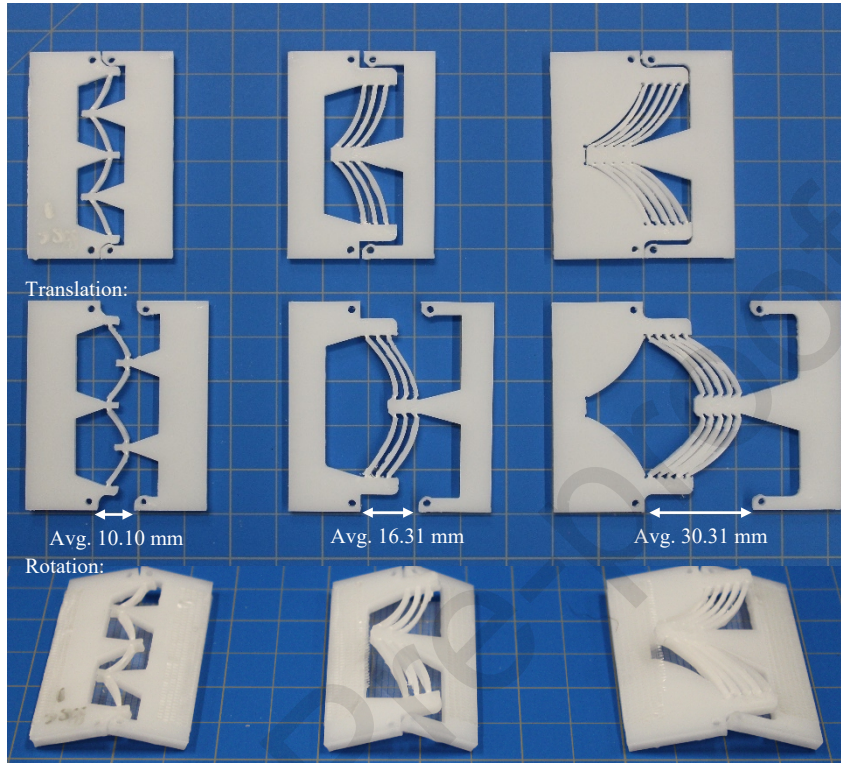


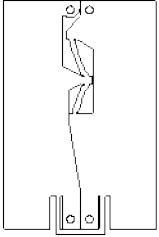
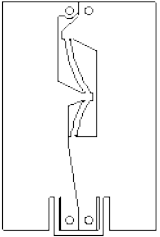
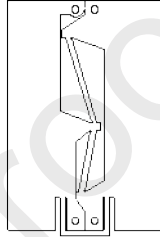
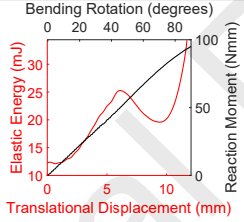
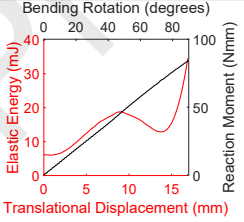
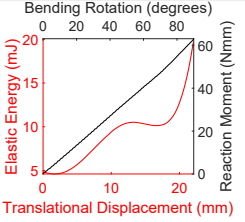
Figure 11. Three rectangle LRBT joints and their translational and rotational deformations.

465 3.2 The Triangle LRBT Joints

As shown in Section 2, some target hinge openings are triangle shapes. Drawing procedures for generating triangle LRBT joints with specified openings are given in Figure 25 in Appendix A. The bottom corners of the plates must be connected while still allowing in- and out-of-plane rotation. This can be achieved by connecting the bottom corners with cutout beams as shown in Figure 12 and Figure 25(c), producing a compliant pin-joint connection. 470 Plots from numerical simulations show that they are linear-rotational and bistable-translational.

475

Table 2 Three triangle LRBT joints.

Target Opening g_t	9.8 mm	14.1 mm	20.5 mm
Design			
Opening size exp. (mm)	10.34	13.98	19.56
Avg. error	5.51%	-0.89%	-4.59%
Num. translation (stage 2) and bending plots			



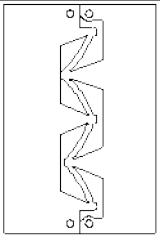
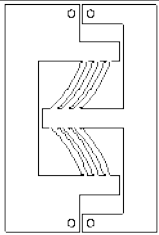
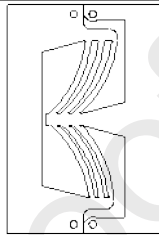
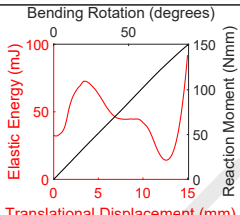
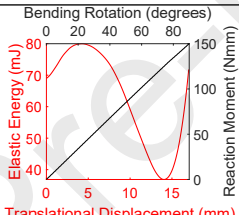
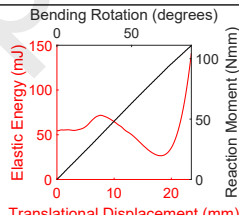
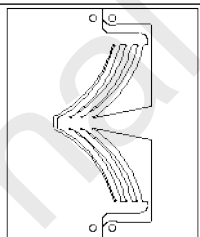
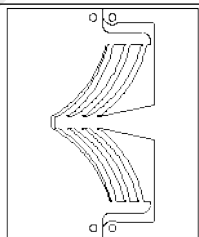
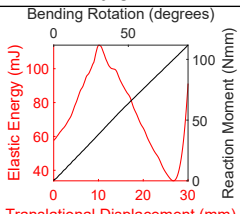
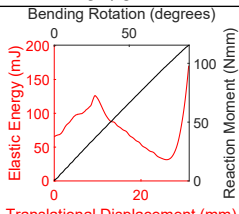
480

Figure 12. Three triangle LRBT joints and their translational and rotational deformations.

3.3 The Trapezoid LRBT Joints

Some target openings take trapezoidal shapes. Drawing procedures of
 485 generating trapezoid LRBT joints with specified openings are given in
 Figure 26 and Figure 27 in Appendix A. Designs with different openings
 are presented in Table 3 and Figure 13. A maximum error of 10.84% is
 observed. The designs are linear-rotational and bistable-translational as
 observed in plots of numerical simulations, where the translational
 490 displacement is measured as the average of g_1 and g_2 .

Table 3 Five trapezoidal LRBT joints.

Target Opening g_1 and g_2	14.3 mm 9.8 mm	16.7 mm 15.1 mm	23.5 mm 14.1 mm
Design			
Opening size exp. (mm)	13.97 9.88	15.70 15.08	21.37 13.51
Avg. error	-2.34% 0.77%	-6.02% -0.17%	-9.06% -4.22%
Num. translation (stage 2) and bending plots			
Target Opening g_1 and g_2	29.7 mm 25.5 mm	30.1 mm 21.2 mm	
Design			
Opening size exp. (mm)	28.03 22.74	27.96 22.43	
Avg. error	-5.64% -10.84%	-7.11% 5.78%	
Num. translation (stage 2) and bending plots			

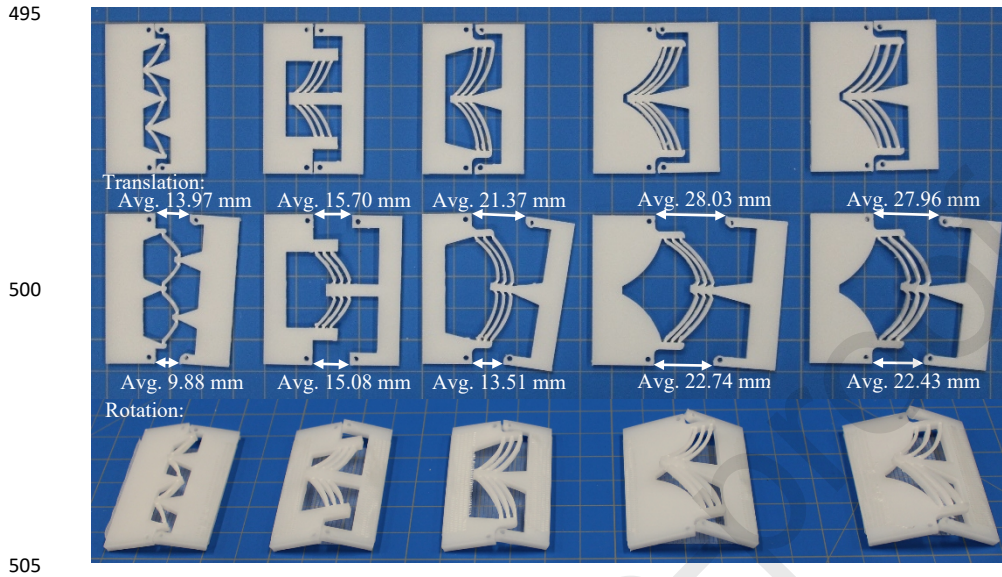


Figure 13. Five trapezoidal LRBT joints and their translational and rotational deformations.

This section has presented designs of LRBT joints that can provide the specified opening (rectangular, triangular, or trapezoidal shape) and verified that they are linear elastic in rotation and bistable in translation.

4. Integration into reconfigurable surfaces

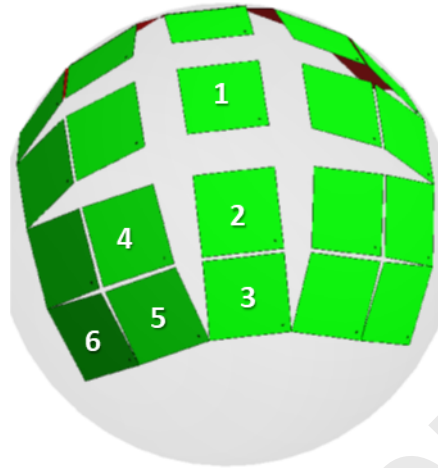
Two square (tile) arrangements, 5 by 5 and 7 by 7, were produced using the technique introduced in Section 2. Corresponding LRBT joints were designed and put into arrays to form the 2D cutting patterns. A laser cutter was used to cut the structures from 3.175 mm thick polypropylene copolymer sheets. An actuation setup was developed to morph the prototype between all 4 target configurations using 3 actuators (2 cables and 1 slider). To characterize the target shapes of the prototype, 3D

520 scanning was used, showing close agreement with the ideal target shapes.
High resolution pictures and actuation videos can be found in the
supplementary material.

4.1 *The 5 by 5 Pattern*

525 4.1.1 *Arrangement of Square Tiles on a Sphere and the 2D Cutting Pattern*

A 5 by 5 pattern with square size of 60 mm and radius of 168 mm is
generated and shown in Figure 14 where different square tiles are marked
with numbers. Openings between each pair of square tiles are given in
530 Table 4 and corresponding joints are chosen from Table 1, Table 2, and
Table 3. A 2D cutting pattern can be generated as shown in Figure 15
where there are 4 holes at corners of each square for mounting antenna
tiles. The widths of some hinge openings are approximately the thickness
of the material, so they are jointed simply by torsional beams (LET joints)
535 as almost no translational movement is needed. Redundant material is
cut away to save weight. The outcome is one continuous structure.



540 Figure 14. Arrangement of 5 by 5 square tiles with 60 mm width on a sphere with radius 168 mm, and there are 6 different positions of square tiles (based on symmetry) that are marked by numbers.

545 Table 4 Opening sizes between adjacent square tiles measured from the arrangement of squares in Figure 14.

Pair of Square Tiles	Opening Type	Opening Size (mm)
1-2	Rectangle	32.5
2-3	Rectangle	2.9
2-4	Trapezoidal	$g_1=30.1$ $g_2= 21.2$
3-5	Triangle	20.5
4-5	Trapezoidal	$g_1=3.8$ $g_2= 3.0$
5-6	Triangle	3.7

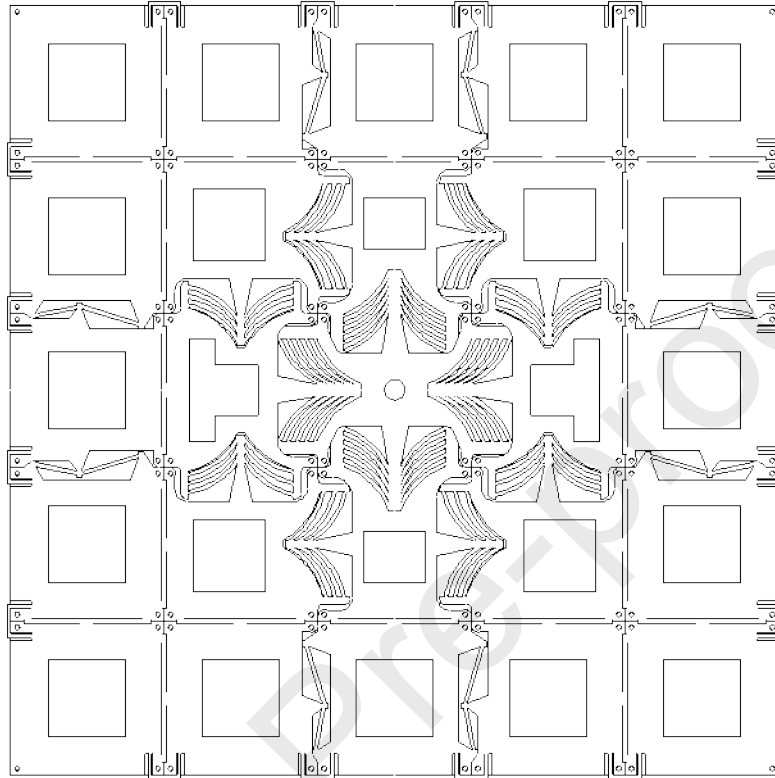


Figure 15. The 5 by 5 cutting pattern of the resultant structure that can reconfigure to all 4 target configurations presented in Figure 1.

550

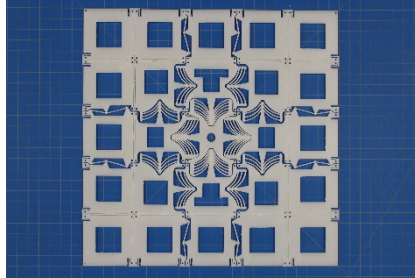
4.1.2 Manufacturing, Actuation, and Shape Measurement

It took about 2 hours to cut the structure, which produced the reconfigurable surface shown in Figure 16. The structure in the flat configuration is like an elastic plate which can be folded along the edges of square tiles. It is stable by internal energy at flat and spherical configurations (Figure 16(a)(c)) and can be stable at cylindrical configurations by actuation (which is taped at the back of the structure in Figure 16(b)). The out-of-plane stiffness of the structure at flat configuration is provided by the rigid plate (that it conforms to at the

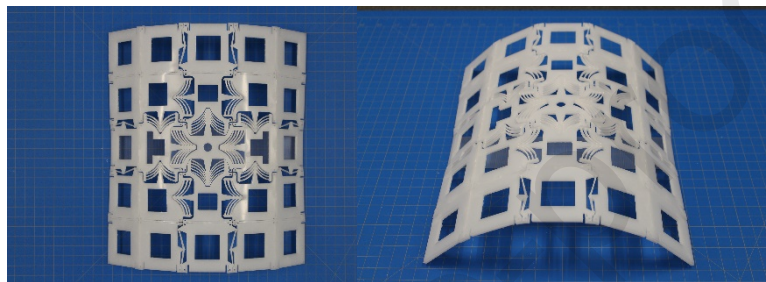
555

560 back) and contacts introduced by antenna tiles (to be installed at the
front). Prestress is created at cylindrical and spherical configurations due
to bending deformation of all LRBT joints, which increases the out-of-
plane stiffness of the structure. Thicker substrates introduce larger
prestress and correspondingly larger stiffness.

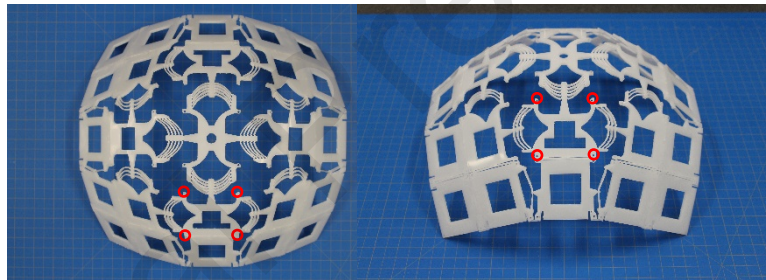
565 Actuation setup was developed and shown in Figure 17. There are
three actuators, including 2 cables and 1 slider. A rigid plate holding 4
pulleys supports the two cables. The plate can slide along a rigid rod (a
T-slotted framing rail). The center square tile of the reconfigurable
surface is connected to the top of the rigid rod, and the bottom of the rod
570 is clamped to the foundation.



(a)

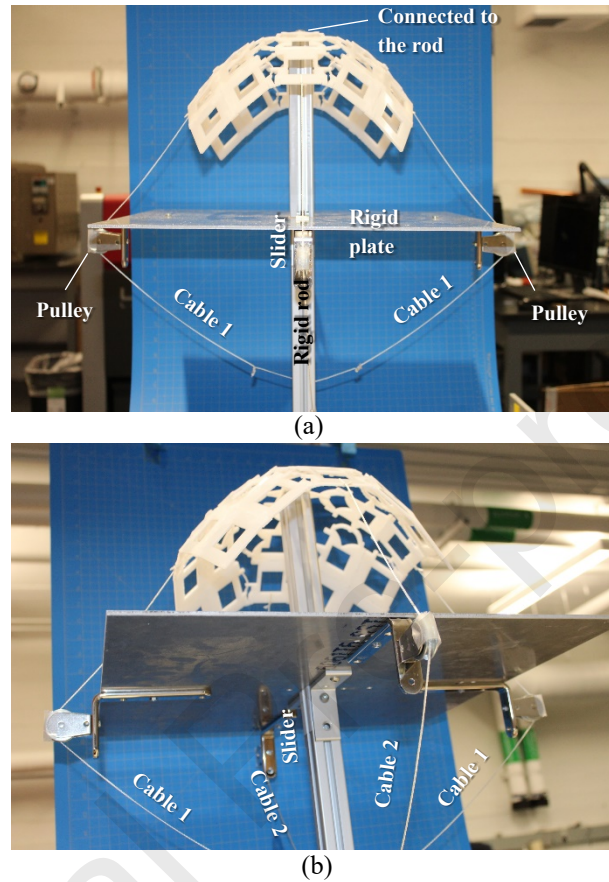


(b)



(c)

Figure 16. The 5 by 5 reconfigurable surface in (a) flat configuration (stable), (b) cylindrical configuration (held stable by tape), and (c) spherical configuration (stable).



575

Figure 17. The actuation setup that consists of 2 cables and 1 slider in (a) side view and (b) bottom view.

Actuation is shown in Figure 18. Here, the structure morphs in
 580 between 4 target configurations by actuating 2 cables and 1 slider. In the flat configuration (Figure 18(a)), the structure conformed to the shape of the rigid flat plate. When lowering the rigid plate and pulling 1 cable (and holding it), cylindrical configurations (Figure 18(c)(d)) could be achieved where LRBT joints worked as elastic torsional hinges. While
 585 pulling 2 cables further, all LRBT joints were snapped open, forming the spherical configuration (Figure 18(f)). In this configuration, the structure

was stable by itself (the cables did not need to held). Then, sliding the rigid plate up, the structure was compressed between the top of the rigid rod and the top surface of the rigid plate, which closed all the LRBT joints and the structured snapped to the flat configuration (Figure 18(g)(h)(i)). A video of the actuation sequence is provided in the supplementary material.

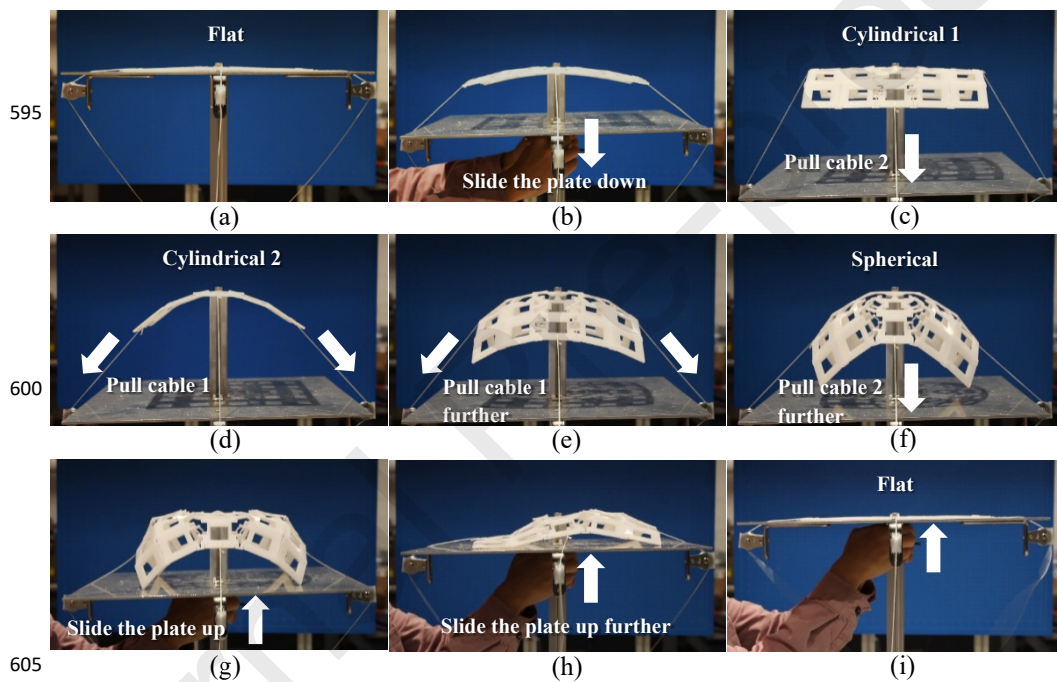
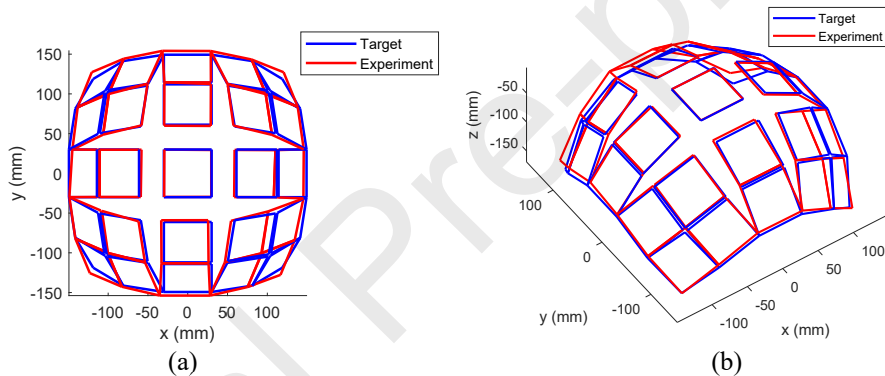


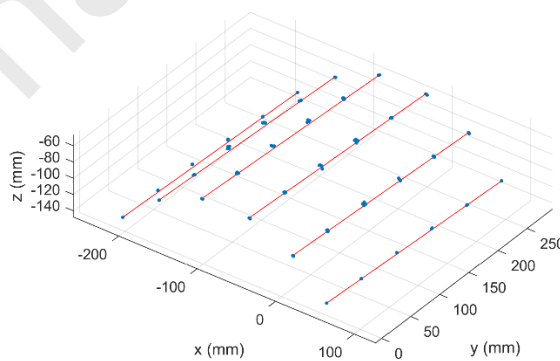
Figure 18. Morphing in between 4 target configurations by actuating 2 cables and 1 slider.

The spherical shape was measured by 3D scanning and was compared to the target shape, which is shown in Figure 19. Four corners of each square tile, which are circled in red for one square tile in Figure 16(c), were regarded as reference points and measured. As shown in Figure 19, the experimental configuration is slightly longer in y direction and

shorter in x direction. Four corners of the structure are slightly bulged
 615 out compared to the target shape. The maximum deviation (in terms of
 the distance) from the target coordinate is 14.04 mm, and the averaged
 deviation is 6.22 mm. The width of the ideal structure is 300 mm, giving
 a maximum relative error of 4.7% and an averaged relative error of 2.1%.
 The 3D scanned cylindrical configuration is given in Figure 20 where
 620 good uniformity is observed. The experimental shape can be influenced
 by the residual stress in the elastic beams, self-weight, plasticity induced
 during actuation, and manufacturing imperfections.



625 Figure 19. Comparison of 3D scanned spherical shape and the target shape in (a) top view and (b) side view.



630 Figure 20. The 3D scanned cylindrical shape is represented by blue dots, and red ruling lines are to help discern the shape.

4.2 The 7 by 7 Pattern

The generality of the LRBT design process is demonstrated by constructing a structure composed of a 7 by 7 array of tiles. Figure 21 shows the 7 by 7 square arrangement on a sphere with tile width of 60 mm and radius of 240 mm. Corresponding LRBT joints can be designed and placed into a 2D array as shown in Figure 22(a). Cylindrical and spherical configurations are presented in Figure 22(b) and (c) which visually show good consistency.



640

Figure 21. Arrangement of 7 by 7 squares on a sphere.

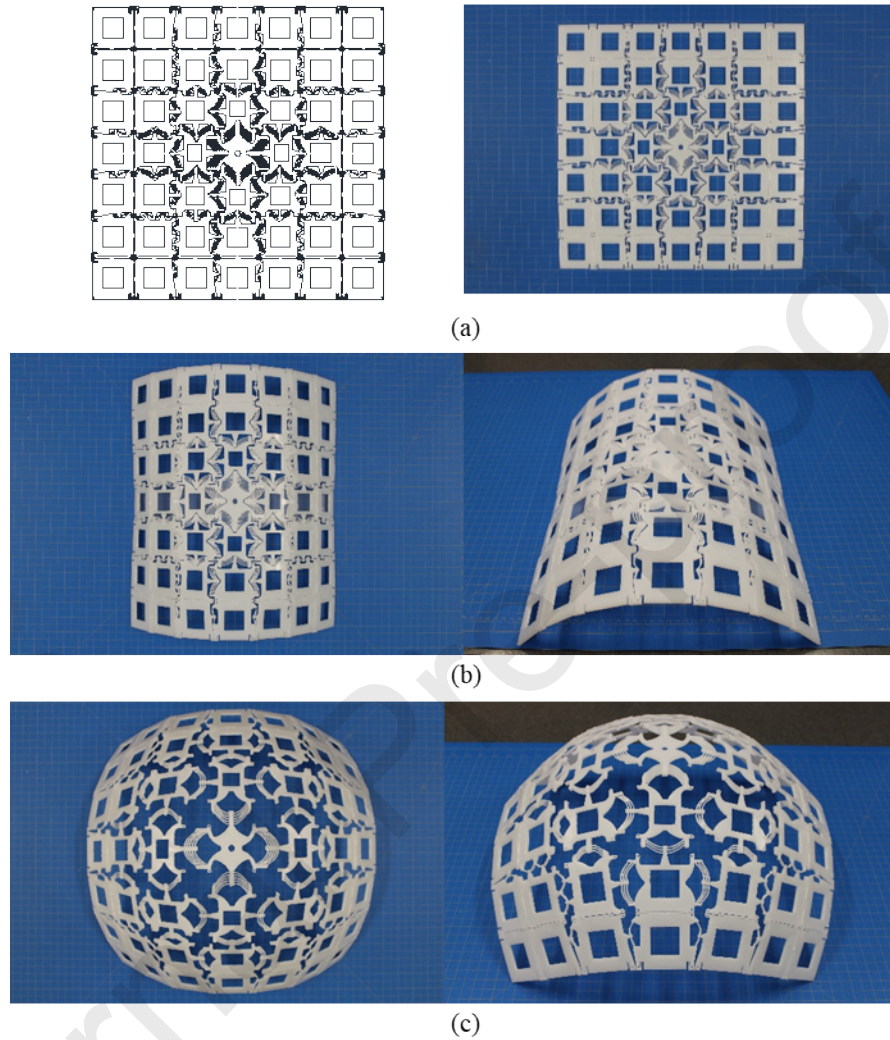


Figure 22. The 7 by 7 reconfigurable surface in (a) flat, (b) cylindrical, and (c) spherical configurations.

645

5. Conclusion

This paper has proposed a new class of reconfigurable surfaces consisting of rigid elements (tiles) connected by novel compliant joints. These joints can work as torsional hinges that enable isometric

650 transformation, such as origami folding, between connected rigid pieces. When actuated specifically, these joints can work as bistable translational springs that bring metric-changing transformation between connected rigid pieces. When the bistability of joints is designed accordingly, desired metric-changing configurations, such as specified
655 spherical shapes, can be achieved with simple actuation. A specific example of a reconfigurable surface with square tiles that can morph between flat, cylindrical (in two different directions), and spherical configurations is presented. One advantage of this method is its convenience in manufacturing. Another merit is its designable (and high)
660 stiffness at all target configurations due to bistability and prestress in the joints. The prestress comes from the bending deformation of LRBT joints in cylindrical and spherical joints, and thicker substrates introduce larger prestress and correspondingly larger stiffness.

Theoretical aspects of this research are left for future work. Since
665 many bistable elements are employed in a 2D array, a number of bifurcations and intermediate stable states can be created [58]. To design a reliable reconfigurable structure and the corresponding actuation scheme, a theoretical framework that connects the design parameters to the energy landscape of the structure is needed. The framework (similar
670 to the one given in [41]) shall unveil the interaction among kinematic constraints, energy profile of each joint, and the overall energy landscape.

Further research could also explore the possibility of removing the no-shear condition in Section 2 to achieve more uniform and compact
675 arrangements of tiles, as shown in Figure 27. Detailed characterization

of mechanical properties of the reconfigurable surface would also be of interest.

This concept can be applied to different tile shapes and different target configurations. The general steps are the same with the outline of this paper: (1) identify the compact tile arrangements in 2D where origami-like folding is allowed between tiles to generate isometric transformation; (2) arrange the tiles on a 3D target surface with reasonable adjacency; (3) measure gap types and sizes in between tiles on that 3D surface; (4) design LRBT joints accordingly for all the gaps; (5) assemble LRBT joints and tiles into a continuous 2D structure that can reconfigure to the 3D target shape through metric-changing transformation.

Other features, such as “bistable-rotational” elements [59], can be integrated. Other applications, such as wearable electronics and robotics, can be explored as well.

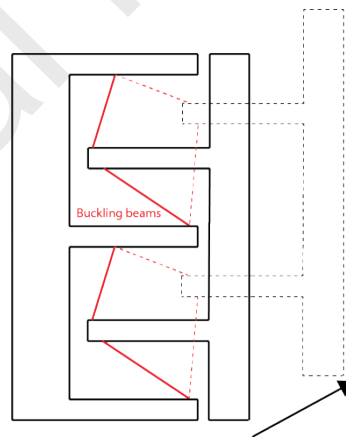


Figure 23. A LRBT joint that has translation containing “shear” along the hinge direction.

695 **Acknowledgements**

Discussions with David E. (Elliott) Williams, Professor Sergio Pellegrino, and the team of the AFOSR MURI project *Universal Electromagnetic Surface: Exploiting active electronics and active origami to generate a programmable electromagnetic response* are acknowledged. This paper is based upon work supported by the Air Force Office of Scientific Research under award number FA9550-18-1-0566 directed by Dr. Ken Goretta.

Appendix A

705 *Design with A Specified Rectangle Opening*

As shown in Section 2, a target opening size is given, and the corresponding LRBT joint design needs to be generated. This procedure is demonstrated in this subsection for rectangular openings. Another requirement (other than matching the specified translational opening) is that the center of rotation during bending occurs at the boundary of two connected plates. An example of generating the design shown in Figure 5(a) is given. The red rectangle in Figure 24(a) is the target rectangle opening where the red dotted line is the vertical bisector of AD. The blue dotted line is the vertical bisector of AC, and it is the center of rotation during bending. With specified margins due to connecting and mounting requirements (of antenna tiles), the position of beams can be determined. A radius of 30 mm is added to beams reduce the force required to open the hinge. Four holes are for mounting antenna tiles (later). The resultant

structure is expected to (1) open to the size of the red rectangle when
 720 pulled laterally and (2) to rotate along the blue dotted line when bent.

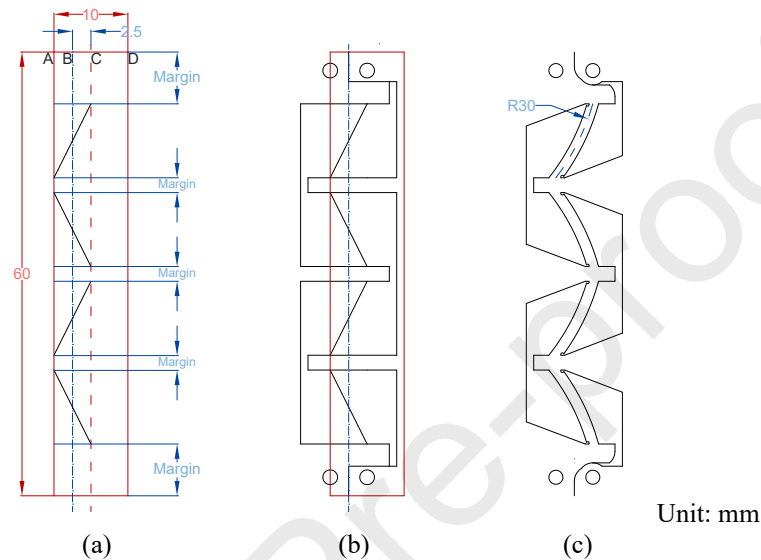


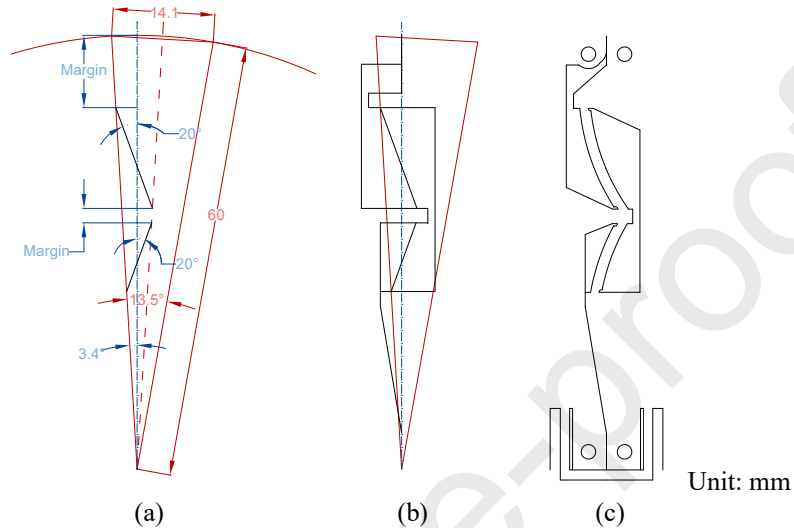
Figure 24. The drawing procedure of a LRBT joint to match a given rectangle opening and center of rotation.

725

Design with A Specified Triangle Opening

In this subsection, procedures for generating LRBT joint designs that
 open into target triangle shapes are provided. In Figure 25, the red
 730 triangle is the target translational opening, and the blue dotted line is the
 center of rotation during bending. Dimensions of margins (≥ 2 mm) are
 chosen. A 20° angle between the beam and the blue dotted line is chosen
 to satisfy Eqs. (13)(14)(15). The bottom part of the structure connects
 the two plates with three beams. With the help of contacts, the bottom
 735 part equivalently produces a compliant pin-joint connection. Three
 designs produced according to this drawing procedure (Figure 25) are

given in Table 2 and Figure 12. Curvature is not added for $g_i=20.5$ mm as the beams are slender.



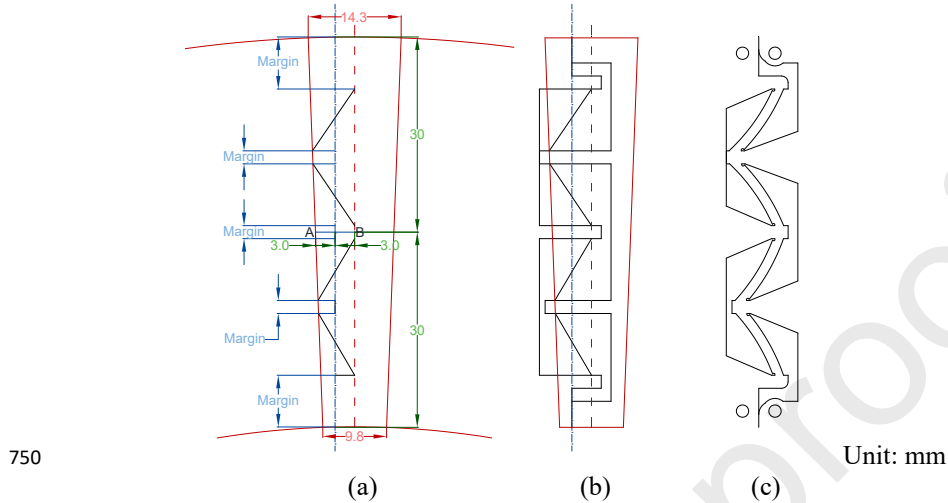
740

Figure 25. The drawing procedure of a LTBT joint to match a specified triangle opening and the center of rotation.

Design with A Specified Trapezoidal Opening

745

Some target openings take trapezoidal shapes and this subsection introduces a procedure to generate such openings. When the opening is small, the drawing procedure given in Figure 26 is employed, where the red trapezoid is the target opening. The blue dotted line is the vertical bisector of AB and is the center of rotation during bending.



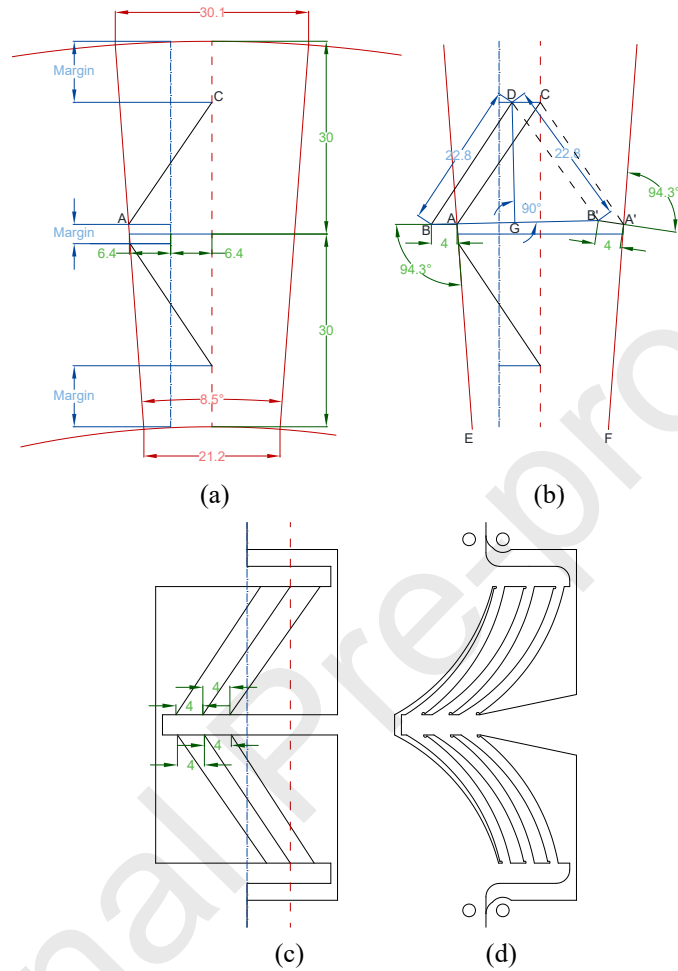
(a) (b) (c)

Figure 26. The drawing procedure of a LTBT joint to match a given small trapezoidal opening and center of rotation.

755

When the opening is large, where Eq. (13)(14)(15) cannot be satisfied using the pattern shown in Figure 26, the drawing scheme shown in Figure 27 is employed. Line segment AB has a length of 4 mm and is perpendicular to the blue dotted line. $|AC| = |A'C|$ defines A'. $|AB| = |A'B'|$ and $\angle BAE = \angle B'A'F$ give B'. DG is the vertical bisector of line segment B'B, which gives point D. As a result, $|BD| = |B'D|$ and BD is the position of an elastic beam. Similarly, the positions of other elastic beams can be worked out, leading to non-symmetric beams.

760



765

Figure 27. The drawing procedure of a LTBT joint to match a given large trapezoidal opening and center of rotation.

770

Supplementary material

Supplementary material includes all the drawings in a dxf file and slides that contain pictures and videos of prototypes.

References

- 775 1. Yao, S. and S.V. Georgakopoulos, *Origami Segmented Helical Antenna With Switchable Sense of Polarization*. IEEE Access, 2018. **6**: p. 4528-4536.
2. Wu, Y., et al. *3D Printed Modular Origami Inspired Dielectrics for Frequency Tunable Antennas*. in *2019 IEEE International Symposium on Antennas and Propagation and USNC-URSI Radio Science Meeting*. 2019.
- 780 3. Chaudhari, S., et al. *A New Class of Reconfigurable Origami Antennas Based on E-Textile Embroidery*. in *2018 IEEE International Symposium on Antennas and Propagation & USNC/URSI National Radio Science Meeting*. 2018.
4. Lee, S., et al., *Frequency-Reconfigurable Antenna Inspired by Origami Flasher*. IEEE Antennas and Wireless Propagation Letters, 2019. **18**(8): p. 1691-1695.
- 785 5. Khan, M.R., et al. *Origami-Enabled Frequency Reconfigurable Dipole Antenna*. in *2019 IEEE International Symposium on Antennas and Propagation and USNC-URSI Radio Science Meeting*. 2019.
6. Fuchi, K., et al., *Origami Tunable Frequency Selective Surfaces*. IEEE Antennas and Wireless Propagation Letters, 2012. **11**: p. 473-475.
- 790 7. Fuchi, K., et al. *Frequency tuning through physical reconfiguration of a corrugated origami frequency selective surface*. in *2017 IEEE International Symposium on Antennas and Propagation & USNC/URSI National Radio Science Meeting*. 2017.
8. Abadi, S.M.A.M.H., J.H. Booske, and N. Behdad, *Exploiting Mechanical Flexure as a Means of Tuning the Responses of Large-Scale Periodic Structures*. IEEE Transactions on Antennas and Propagation, 2016. **64**(3): p. 933-943.
- 795 9. Russo, N.E., C.L. Zekios, and S.V. Georgakopoulos. *Origami Multimode Ring Antenna Based on Characteristic Mode Analysis*. in *2019 IEEE International Symposium on Antennas and Propagation and USNC-URSI Radio Science Meeting*. 2019.
- 800 10. Liu, X., S. Yao, and S.V. Georgakopoulos. *Mode reconfigurable bistable spiral antenna based on kresling origami*. in *2017 IEEE International Symposium on Antennas and Propagation & USNC/URSI National Radio Science Meeting*. 2017.
- 805 11. Georgakopoulos, S.V. *Reconfigurable Origami Antennas*. in *2019 International Applied Computational Electromagnetics Society Symposium (ACES)*. 2019.
- 810 12. Shah, S.I.H. and S. Lim, *Thermally Beam-Direction- and Beamwidth-Switchable Monopole Antenna Using Origami Reflectors With Smart Shape Memory Polymer Hinges*. IEEE Antennas and Wireless Propagation Letters, 2019. **18**(8): p. 1696-1700.
13. Carrara, G.P., et al. *A Deployable and Reconfigurable Origami Antenna for Extended Mobile Range*. in *2019 IEEE International Symposium on Antennas and Propagation and USNC-URSI Radio Science Meeting*. 2019.
- 815

14. Seiler, S.R., et al. *An Origami Inspired Circularly-Polarized Folding Patch Antenna Array*. in *2018 IEEE International Symposium on Antennas and Propagation & USNC/URSI National Radio Science Meeting*. 2018.
- 820 15. Zhu, C. and B. Feng. *A Dual-Polarized Antenna Using an Origami Structure for 5G Emergency Communications*. in *2019 International Workshop on Electromagnetics: Applications and Student Innovation Competition (iWEM)*. 2019.
16. Sessions, D.M., et al. *Folding, Tessellation, and Deployment of an Origami-Inspired Active-Material-Enabled Self-Folding Reflector Antenna*. in *2018 IEEE International Symposium on Antennas and Propagation & USNC/URSI National Radio Science Meeting*. 2018.
- 825 17. Costantine, J., et al., *UHF Deployable Helical Antennas for CubeSats*. IEEE Transactions on Antennas and Propagation, 2016. **64**(9): p. 3752-3759.
18. Shah, S.I.H., M.M. Tentzeris, and S. Lim, *A Deployable Quasi-Yagi Monopole Antenna Using Three Origami Magic Spiral Cubes*. IEEE Antennas and Wireless Propagation Letters, 2019. **18**(1): p. 147-151.
- 830 19. Williams, D.E., et al. *Origami-Inspired Shape-Changing Phased Array*. in *50th European Microwave Conference (EuMC)*. 2020 (to be published). Utrecht, The Netherlands.
- 835 20. Guy, R.F.E. *Spherical coverage from planar, conformal and volumetric arrays*. in *IEE National Conference on Antennas and Propagation*. 1999.
21. Kildal, P., E. Martini, and S. Maci, *Degrees of Freedom and Maximum Directivity of Antennas: A bound on maximum directivity of nonsuperreactive antennas*. IEEE Antennas and Propagation Magazine, 2017. **59**(4): p. 16-25.
- 840 22. Gustafsson, M. and M. Capek, *Maximum Gain, Effective Area, and Directivity*. IEEE Transactions on Antennas and Propagation, 2019. **67**(8): p. 5282-5293.
23. Hawkes, E., et al., *Programmable matter by folding*. Proceedings of the National Academy of Sciences, 2010. **107**(28): p. 12441.
- 845 24. Paik, J.K., et al., *Robotic Origamis: Self-morphing Modular Robot*.
25. Peraza-Hernandez, E.A., D.J. Hartl, and R.J. Malak Jr, *Design and numerical analysis of an SMA mesh-based self-folding sheet*. Smart Materials and Structures, 2013. **22**(9): p. 094008.
- 850 26. Gattas, J.M., W. Wu, and Z. You, *Miura-Base Rigid Origami: Parameterizations of First-Level Derivative and Piecewise Geometries*. Journal of Mechanical Design, 2013. **135**(11).
27. Chen, Y., et al., *Symmetric waterbomb origami*. Proceedings of the Royal Society A: Mathematical, Physical and Engineering Sciences, 2016. **472**(2190): p. 20150846.
- 855 28. Tachi, T., *Designing Freeform Origami Tessellations by Generalizing Resch's Patterns*. Journal of Mechanical Design, 2013. **135**(11).
29. Li, Y., *Motion Paths Finding for Multi-Degree-of-Freedom Mechanisms*. International Journal of Mechanical Sciences, 2020: p. 105709.
- 860 30. Magliozzi, L., et al., *On the design of origami structures with a continuum of equilibrium shapes*. Composites Part B: Engineering, 2017. **115**: p. 144-150.
31. Choi, G.P.T., L.H. Dudte, and L. Mahadevan, *Programming shape using kirigami tessellations*. Nature Materials, 2019. **18**(9): p. 999-1004.

- 865 32. Chiang, Y.-C., S. Mostafavi, and H. Bier, *Assembly of shells with bi-stable mechanism*. 2018: Proceedings of Advances in Architectural Geometry 2018 (AAG 2018).
33. Chen, T., J. Mueller, and K. Shea, *Integrated Design and Simulation of Tunable, Multi-State Structures Fabricated Monolithically with Multi-Material 3D Printing*. Scientific Reports, 2017. **7**(1): p. 45671.
- 870 34. Kim, Y., et al., *Printing ferromagnetic domains for untethered fast-transforming soft materials*. Nature, 2018. **558**(7709): p. 274-279.
35. Hajiesmaili, E. and D.R. Clarke, *Reconfigurable shape-morphing dielectric elastomers using spatially varying electric fields*. 2019. **10**(1): p. 183.
36. Plucinsky, P., et al., *Patterning nonisometric origami in nematic elastomer sheets*. Soft Matter, 2018. **14**(16): p. 3127-3134.
- 875 37. Guseinov, R., et al., *Programming temporal morphing of self-actuated shells*. Nature Communications, 2020. **11**(1): p. 237.
38. Ma, M., et al., *Bio-Inspired Polymer Composite Actuator and Generator Driven by Water Gradients*. Science, 2013. **339**(6116): p. 186.
- 880 39. Page, D.J., *Reconfigurable Surface*, U.S. Patent, Editor. Jun. 7, 2005: US. p. US 6,903,871 B2.
40. Leithinger, D., et al., *Direct and gestural interaction with relief: a 2.5D shape display*, in *Proceedings of the 24th annual ACM symposium on User interface software and technology*. 2011, Association for Computing Machinery: Santa Barbara, California, USA. p. 541–548.
- 885 41. Li, Y. and S. Pellegrino, *A Theory for the Design of Multi-Stable Morphing Structures*. Journal of the Mechanics and Physics of Solids, 2019: p. 103772.
42. Jacobsen, J.O., et al., *Lamina Emergent Torsional (LET) Joint*. Mechanism and Machine Theory, 2009. **44**(11): p. 2098-2109.
- 890 43. Wilding, S.E., L.L. Howell, and S.P. Magleby, *Introduction of planar compliant joints designed for combined bending and axial loading conditions in lamina emergent mechanisms*. Mechanism and Machine Theory, 2012. **56**: p. 1-15.
44. Qiu, J., J.H. Lang, and A.H. Slocum. *A centrally-clamped parallel-beam bistable MEMS mechanism*. in *Technical Digest. MEMS 2001. 14th IEEE International Conference on Micro Electro Mechanical Systems (Cat. No.01CH37090)*. 2001.
- 895 45. Zhao, J., et al., *Post-buckling and Snap-Through Behavior of Inclined Slender Beams*. Journal of Applied Mechanics, 2008. **75**(4).
- 900 46. Zhang, K., et al., *Origami silicon optoelectronics for hemispherical electronic eye systems*. Nature Communications, 2017. **8**(1): p. 1782.
47. Ko, H.C., et al., *A hemispherical electronic eye camera based on compressible silicon optoelectronics*. Nature, 2008. **454**(7205): p. 748-753.
48. Huang, Y., et al., *Assembly and applications of 3D conformal electronics on curvilinear surfaces*. Materials Horizons, 2019. **6**(4): p. 642-683.
- 905 49. Callens, S.J.P. and A.A. Zadpoor, *From flat sheets to curved geometries: Origami and kirigami approaches*. Materials Today, 2018. **21**(3): p. 241-264.
50. Rus, D. and M.T. Tolley, *Design, fabrication and control of origami robots*. Nature Reviews Materials, 2018. **3**(6): p. 101-112.

- 910 51. Zhakypov, Z. and J. Paik, *Design Methodology for Constructing Multimaterial Origami Robots and Machines*. IEEE Transactions on Robotics, 2018. **34**(1): p. 151-165.
52. Chen, T., et al., *Harnessing bistability for directional propulsion of soft, untethered robots*. Proceedings of the National Academy of Sciences, 2018. **115**(22): p. 5698-5702.
- 915 53. Abaqus, *Abaqus Documentation Version 6.13*. Dassault Systems SIMULIA corp., Providence, RI, USA, 2013.
54. Leclerc, C., et al., *Characterization of Ultra-Thin Composite Triangular Rollable and Collapsible Booms*, in *4th AIAA Spacecraft Structures Conference*. 2017, American Institute of Aeronautics and Astronautics.
- 920 55. Ferraro, S. and S. Pellegrino, *Self-Deployable Joints for Ultra-Light Space Structures*, in *2018 AIAA Spacecraft Structures Conference*. 2018, American Institute of Aeronautics and Astronautics.
56. Gomm, T., L.L. Howell, and R.H. Selfridge, *In-plane linear displacement bistable microrelay*. Journal of Micromechanics and Microengineering, 2002. **12**(3): p. 257-264.
- 925 57. Delimont, I.L., S.P. Magleby, and L.L. Howell, *Evaluating Compliant Hinge Geometries for Origami-Inspired Mechanisms*. Journal of Mechanisms and Robotics, 2015. **7**(1).
- 930 58. Puglisi, G. and L. Truskinovsky, *Mechanics of a discrete chain with bi-stable elements*. Journal of the Mechanics and Physics of Solids, 2000. **48**(1): p. 1-27.
59. Jeong, H.Y., et al., *3D printing of twisting and rotational bistable structures with tuning elements*. Scientific Reports, 2019. **9**(1): p. 324.

935